A15 phase Ta_3Sb thin films: Direct synthesis, charge transport, and spin-orbit torque

J. S. Jiang,[1,*] Qianheng Du,[1] Yi Li,[1] Ulrich Welp,[1] Ramakanta Chapai,[1] Hanu Arava,[1] Yuzi Liu,[2] Yue Li,[1] John Pearson,[1] Ralu Divan,[2] Anand Bhattacharya,[1] and Hyowon Park[1,3]

[1]*Materials Science Division, Argonne National Laboratory, Lemont, Illinois 60493, USA*

[2]*Nanoscience and Technology Division, Argonne National Laboratory, Lemont, Illinois 60493, USA*

[3]*Department of Physics, University of Illinois at Chicago, Chicago, Illinois 60607, USA*

(Received 31 March 2025; accepted 4 August 2025; published 20 August 2025)

Ta_3Sb is one of the A15 compounds that have been predicted to have giant spin Hall conductivities due to the gapped Dirac-like band crossings in their electronic structures. We use co-sputtering to directly synthesize thin films of Ta_3Sb and identify a large window of Ta:Sb flux ratio that permits the formation of single-phase A15 structure. These sputtered films have an actual Ta:Sb atomic ratio of 4:1, as determined from Rutherford backscattering spectrometry. Their high resistivity, at the Mott-Ioffe-Regel limit, suggests that the electron mean free path is comparable to interatomic distances. From harmonic Hall and spin-torque ferromagnetic resonance measurements, the intrinsic spin Hall conductivity of thin film Ta_3Sb is estimated to be in the range of -526 to $-1230\ (\hbar/e)$ S/cm at 300 K, lower in magnitude than the predicted value of $-1400\ (\hbar/e)$ S/cm. First-principles calculations of the electronic structure show that the discrepancy is consistent with an increase of the Fermi level due to the nonideal stoichiometry needed to stabilize the A15 structure.

DOI: 10.1103/twfb-d5vd

I. INTRODUCTION

Current-induced spin-orbit torques (SOTs) have become a promising tool in spintronic applications to electrically manipulate magnetic moments with a lateral current [1–3]. Of significant interest in implementing SOT-based technologies is the development of materials capable of efficient charge-spin conversion. The efficiency of converting between a charge current j_c and spin current j_s is characterized by the SOT efficiency $\xi = (2e/\hbar)(j_s/j_c) = T_{\text{int}}\theta_{SH} \equiv T_{\text{int}}\sigma_{SH}/\sigma$, where T_{int}, θ_{SH}, σ_{SH}, and σ are the interfacial spin transparency, spin Hall angle, spin Hall conductivity, and electrical conductivity, respectively. Thus, a large σ_{SH} can lead to a high ξ. Conventional heavy metals such as Pt and β-W have, in their electronic structures, degenerate bands that are split by spin-orbit coupling (SOC). This leads to nonvanishing Berry curvature which, when integrated over the occupied bands, gives rise to large σ_{SH} [4]. Derunova *et al.* [5] point out that a strategy to search for or design new materials with high σ_{SH} is to maximize Berry curvature by having the Fermi level E_F inside as many small-gapped band crossings as possible. They note that for many intermetallic compounds with the A15 structure, due to their crystalline symmetry (space group 223, $Pm\bar{3}n$), the calculated band structures contain Dirac crossings near E_F if SOC is not considered. These crossings become gapped when SOC is included, leading to giant values of σ_{SH}. It is predicted that the A15 phase W_3Ta has a very large σ_{SH} of $-2250\ (\hbar/e)$ S/cm, and enhancements in spin Hall ratio [6] and effective spin Hall angle [7] have been reported when β-W is doped with Ta. Remarkably, the reported enhancements (9% vs 100%) are vastly different despite similar levels (8.5 vs 11 atomic %) of Ta-doping.

The A15 superconductor Ta_3Sb has also been predicted to have a large $\sigma_{SH} = -1400\ (\hbar/e)$ S/cm with an SOC-gapped eightfold degenerate Dirac point near E_F. Moreover, there exist in Ta_3Sb near E_F topologically nontrivial surface states which may become proximitized by the bulk superconductivity, making Ta_3Sb a potential candidate to explore topological superconductivity [5,8,9]. Because of the large difference in the melting points of Ta and Sb, and the high vapor pressure of Sb, direct synthesis of Ta_3Sb has not been possible. Chapai *et al.* [10] synthesized phase-pure powders of A15 Ta_3Sb from the Sb-rich precursor $TaSb_2$ via a lengthy 14-day thermal decomposition process. The superconducting properties and specific heat of Ta_3Sb were studied using pellets pressed from the powders. However, due to the porous nature of the pressed pellets, it was not possible to fabricate the device structures that are necessary for characterizing spin-orbit effects.

In this work, we directly synthesize thin films of Ta_3Sb from elemental sources using the co-sputtering process. We identify a large window of processing conditions that can stabilize single-phase A15 Ta_3Sb, and analyze the structure and charge transport characteristics of the thin films. The chemical composition of thin film Ta_3Sb deviates from the ideal stoichiometry but agrees with that of Ta_3Sb bulk crystals [10] and is as expected from the Ta-Sb equilibrium phase diagram [11]. From harmonic Hall and spin-torque ferromagnetic resonance measurements, we estimate a range for the spin Hall conductivity of Ta_3Sb, which is lower in magnitude than the theoretical prediction. We perform density functional theory calculations for the electronic structure and explain that the discrepancy in spin Hall conductivity is due to the non-ideal stoichiometry of the actual A15-phase Ta_3Sb. We highlight the importance of the location of E_F of realizable

*Contact author: jiang@anl.gov

 ©2025 American Physical Society

A15 materials and discuss possible avenues to optimize their spin Hall conductivity.

II. THIN FILM SYNTHESIS AND STRUCTURAL CHARACTERIZATION

The Ta_3Sb films were grown by magnetron sputtering from elemental Ta and Sb targets onto silicon (100) wafers with a native oxide layer. Both doped (resistivity 10 Ω cm) and intrinsic (resistivity >20 kΩ cm) wafers were used. The choice of substrate had no effect on film growth. The base pressure of the deposition system before growth was better than 3×10^{-9} Torr. The working pressure of the Ar sputter gas was maintained at 3 mTorr. The source fluxes were set with a calibrated quartz microbalance before deposition, and were measured after deposition to ensure there had been no significant drift. Because of the high vapor pressure of Sb, an over-supply of Sb flux was necessary to compensate for losses during film growth. We varied the substrate temperature and the Ta:Sb flux ratio to search for the optimal growth conditions, guided by crystal structure and phase analyses of x-ray diffraction (XRD) measurements. Figure 1 shows the XRD patterns of Ta-Sb films grown at a substrate temperature of 650 °C with the Ta:Sb flux ratio ranging from 3:1 to 1:2. A threshold Ta:Sb flux ratio of approximately 2:1 was needed for the formation of single-phase A15 Ta_3Sb films. Further decreasing the flux ratio by up to a factor of 4 did not produce any detectable impurity phase or change in the lattice constant of the A15 structure. This result points to a film growth process that is similar to the "phase-locking" approach used for preparing A15 Nb_3Sn films [12]: at suitably controlled substrate temperatures, the film composition always settles to the boundary of the A15 phase, while the surplus high-vapor-pressure component (Sn or Sb) simply re-evaporates, thereby allowing for the direct synthesis of homogeneous A15 films without the need to precisely control the source fluxes. Subsequently, we fixed the substrate temperature at 650 °C and the Ta:Sb flux ratio at 3:2 for all depositions. The effective growth rate calculated from deposition times and the film thicknesses as measured with x-ray reflectivity (XRR) was approximately 2 nm/min. The films were cooled to room temperature at a rate of 20 °C/min. Except for the single-layer Ta_3Sb films prepared for composition analyses, all films were capped with 5 nm of MgO before being taken out of vacuum.

Shown in Fig. 1(b) is a representative XRD 2θ-ω scan of an 85 nm-thick Ta_3Sb film measured using Cu K_α radiation. The film is polycrystalline. To make the higher-index diffraction peaks in the 2θ range of 60°–75° more discernable, we intentionally offset ω by 2.5° from θ so as to suppress the strong Si (200) reflection. All the observed diffraction peaks can be indexed to those of Ta_3Sb with the A15 structure. The lattice constant a is determined from the peak positions to be 0.5272 ± 0.0004 nm, which is very similar to the value reported for bulk crystals of Ta_3Sb [10]. Compared with the Ta_3Sb powder diffraction pattern, where the (200) peak has less than half the intensity of the (211) peak, the (200) diffraction peak of the sputtered film is nearly twice as strong as the (211) peak, indicating some (200) texturing in the growth direction. From the full width at half maximum of the diffraction peaks, we estimate the average coherence length

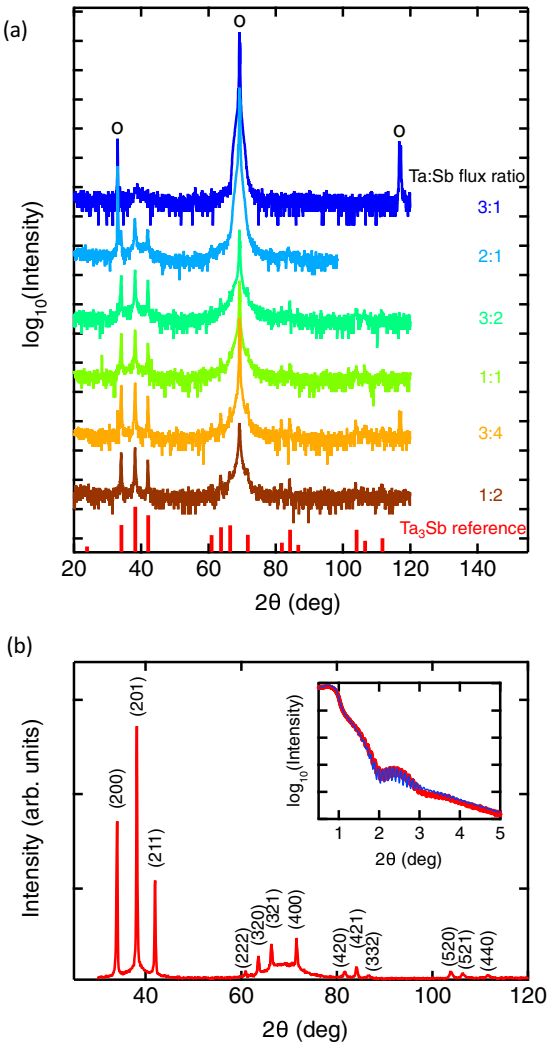

FIG. 1. (a) XRD patterns of Ta-Sb films sputter-grown at various Ta:Sb flux ratios. The patterns are shifted vertically for clarity. The XRD scattering vector is aligned along the surface normal. The diffraction peaks marked with the symbol "o" are due to the silicon substrate. (b) XRD pattern of an 85 nm Ta_3Sb film. Inset: XRR data and fit. The slower modulation in intensity is due to the MgO capping layer.

of the Ta_3Sb crystallites to be about 40 nm in the growth direction. The XRR measurement on an identically grown Ta_3Sb film is shown in the inset of Fig. 1(b). Fitting the data yields a layer thickness of 84.8 nm and a Ta_3Sb/MgO interfacial roughness of 1.2 nm.

Although the XRD pattern and the lattice constant of the sputtered films match those of the A15 Ta_3Sb, their actual chemical composition deviates from that of the ideal stoichiometry. We analyzed the composition of our films using Rutherford backscattering spectrometry (RBS). As shown in Fig. 2, curve-fitting the RBS spectrum taken on a 5.4 nm-thick sputtered Ta_3Sb film yields areal densities of $(43.23\pm0.01)\times10^{15}$ and $(11.04\pm0.01)\times10^{15}$ atoms/cm^2 for Ta and Sb, respectively. This corresponds to a Ta:Sb atomic ratio of 4:1, indicating that the film is Sb-deficient. Similar Sb deficiency has also been reported in bulk crystals and is consistent with the Ta-Sb phase diagram [11], where

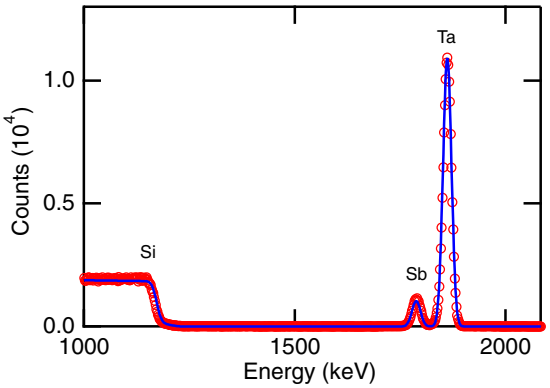

FIG. 2. RBS data and fit of a 5.4 nm Ta_3Sb film.

the A15 phase exists in a narrow homogeneity region that is closer in composition to Ta_4Sb and is characterized by a random mixing of Ta and Sb atoms at the Sb site [10]. As is typically done for A15 compounds that deviate from their ideal stoichiometry, we refer to the sputtered films by their prototypical formula as Ta_3Sb throughout.

To assess the microstructure and compositional uniformity of the sputtered films, we carried out cross-sectional imaging using transmission electron microscopy (TEM) and energy-dispersive x-ray spectroscopy (EDS). The nano-beam electron diffraction was performed in a JEOL 2100f electron microscope, and the EDS mapping was performed in a FEI Talos F200X TEM/STEM. The dark-field (DF) cross-sectional TEM image and nanobeam electron diffraction patterns in Fig. 3(a) demonstrate the microstructure of an 85 nm Ta_3Sb film. In the DF image, a columnar microstructure is visible where grains are differently oriented crystallites, as shown by the indexed nanobeam electron diffraction patterns for select areas. The columnar grains are about 10–20 nm wide and only

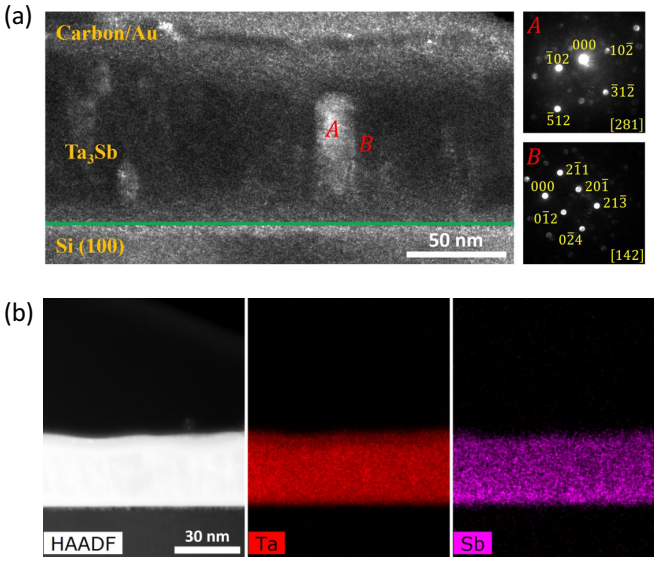

FIG. 3. (a) Dark-field cross-sectional TEM image of an 85 nm Ta_3Sb film. Nanobeam electron diffraction patterns of selected areas A and B are shown. (b) HAADF image and corresponding EDS maps of Ta and Sb showing the elemental distributions.

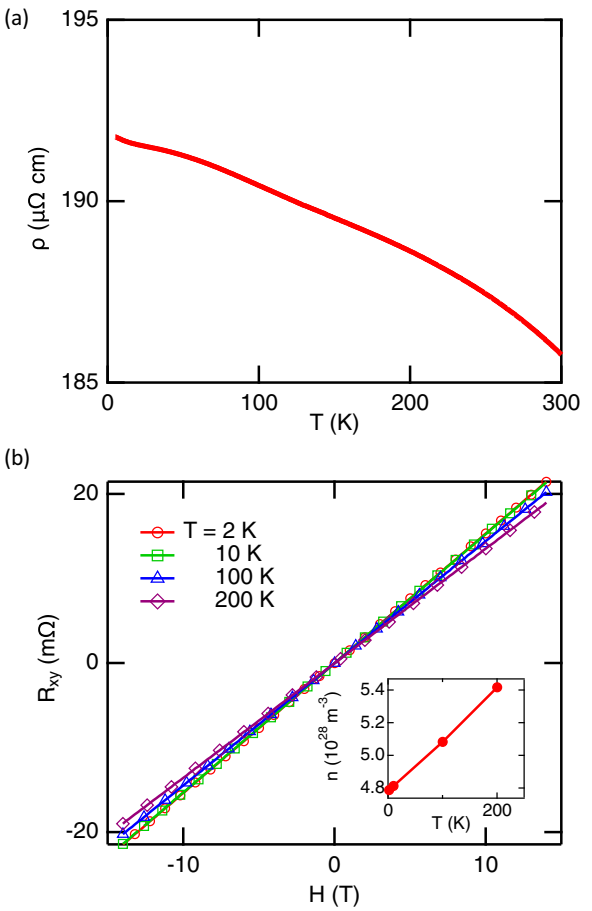

FIG. 4. (a) Electrical resistivity of an 85 nm Ta_3Sb film, plotted as a function of temperature. (b) Hall resistance measured at various temperatures. Inset: The charge carrier density plotted as a function of temperature.

extend to about half the thickness of the film, consistent with the coherence length estimated from the XRD peak widths. In Fig. 3(b), the High-Angle Annular Dark Field (HAADF) image and the corresponding EDS maps of Ta and Sb are displayed. The EDS maps show uniform distribution of the elements. Since Ta_5Sb_4 and $TaSb_2$ are the only other possible Ta-Sb alloy phases, and since both are line compounds, the lack of modulation in EDS intensity at the length scale of grain sizes confirms that our sputtered film is single-phase Ta_3Sb.

III. CHARGE TRANSPORT PROPERTIES

For charge transport properties, films grown on high-resistivity undoped Si were patterned into 6-terminal Hall bar devices using standard optical lithography and argon ion milling. The current channel was nominally 10 μm wide and 40 μm long between the voltage terminals. The width of the voltage terminals was 2 μm. The transport measurements were carried out at temperatures between 50 mK and 300 K in magnetic fields up to 14 T using a Quantum Design PPMS system with a dilution refrigerator insert.

Figure 4(a) shows the electrical resistivity of an 85 nm Ta_3Sb thin film as a function of temperature between 300 K

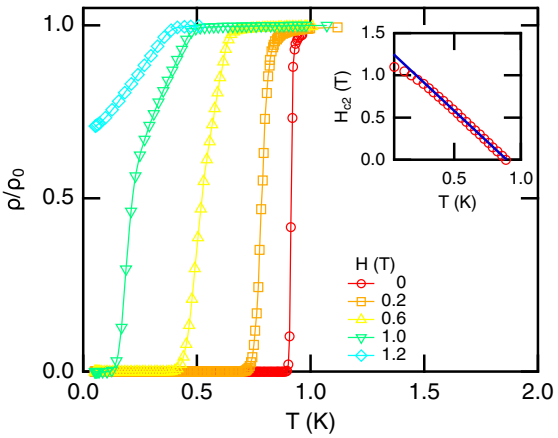

FIG. 5. Normalized resistivity as a function of temperature of an 85 nm Ta_3Sb film showing the superconducting transition at various applied magnetic fields. Inset: The superconducting phase diagram showing the upper critical field as a function of temperature.

and 5 K. The resistivity has a negative temperature coefficient (TCR), increasing from 186 μΩ cm at 300 K to 192 μΩ cm at 5 K. Similarly, the resistivity of a 9.5 nm Ta_3Sb film increases from 224 μΩ cm at 300 K to 237 μΩ cm at 5 K. The very large values of resistivity, comparable to the saturation resistivity of metallic elements and alloys [13], implies that the Ta_3Sb thin films are at the Mott-Ioffe-Regel limit, where the electron mean free path is limited to interatomic distances. The mixing of Ta and Sb atoms at the Sb sites arising from the nonideal stoichiometry could provide the needed strong disorder. The negative TCR could be due to Anderson localization [14], a strong coupling polaronic mechanism [15] or, as originally proposed by Mooij, an increase in the number of charge carriers with temperature [16]. The carrier density in the Ta_3Sb thin films is, indeed, temperature dependent. Shown in Fig. 4(b) are the Hall resistance R_{xy} of the 85 nm Ta_3Sb film as a function of magnetic field measured at various temperatures. R_{xy} is linear with fields as high as 14 T and the slopes are positive, indicating the dominant charge carriers are hole-type. The carrier density is comparable to that of typical metals, increasing slightly with temperature from 4.8×10^{28} m^{-3} at 2 K to 5.4×10^{28} m^{-3} at 200 K [see Fig. 4(b) inset]. This temperature-dependent carrier density might explain the negative TCR in the Ta_3Sb thin films. It is worth nothing that some metals, such as aluminum, also have positive Hall coefficients due to the peculiar shapes of their Fermi surfaces.

In Fig. 5, the resistive superconducting transitions of the Ta_3Sb film measured in various out-of-plane magnetic fields are shown. The superconducting transition temperature T_c, defined as the midpoint of the resistive transition, is 0.887 K at zero field. T_c is progressively suppressed with increasing magnetic field. The upper critical field H_{c2} as a function of temperature is plotted in the inset of Fig. 5. H_{c2} varies linearly with temperature above 0.3 K, but does not exhibit the downward curvature that was observed in Ta_3Sb bulk crystals, indicating that superconductivity in the Ta_3Sb thin films is not confined by grain boundaries and/or voids as it is in the bulk crystals, even though the in-plane extent (10–20 nm) of the crystallites in the thin films is smaller than the grain size (∼45 nm) of the bulk crystals. Extrapolating H_{c2} to zero temperature yields the Ginzburg-Landau upper critical field of $H_{c2}^{GL} = 1.25$ T, which is slightly higher than that of the bulk crystals, consistent with more disorder being present in the Ta_3Sb thin films.

IV. SPIN-ORBIT TORQUE EFFECTS

To quantify the spin Hall angle in the A15 Ta_3Sb thin films, we employed two complementary techniques—harmonic Hall [17] and spin-torque ferromagnetic resonance (ST-FMR) [18]—to measure the current-induced spin-orbit torques in bilayer structures consisting of a Ta_3Sb layer and a soft ferromagnetic layer of $Co_{40}Fe_{40}B_{20}$ (CFB) or $Ni_{81}Fe_{19}$ (Py). The CFB and Py layers were deposited at room temperature after cooling the Ta_3Sb layer without breaking vacuum. The bilayers were then capped with 5 nm of MgO before being taken out of vacuum for lithographic patterning. For harmonic Hall measurements, the bilayers were patterned into the same Hall bar structure as that used for charge transport measurements. For ST-FMR measurements, rectangular microstrips 20 μm × 50 μm in size were patterned from the bilayer films and were integrated with gold co-planar waveguides for radio frequency (RF) excitation [19,20].

In a harmonic Hall measurement, as schematically shown in Fig. 6(a), the spin current induced by an AC current I_{AC} exerts oscillating damping-like (DL) and field-like (FL) effective SOT fields H_{DL} and H_{FL} on the magnetization of the ferromagnet. The oscillation of the magnetization around its equilibrium position gives rise to a second harmonic component in the Hall voltage via the anomalous Hall and planar Hall effects. For in-plane magnetized systems, when an out-of-plane magnetic field H is swept, the second harmonic component of the Hall voltage is given by [17]

$$V_{2\omega} = \frac{I_{AC}R_{AHE}\sin\theta_0\cos\varphi_H}{2(H_K\cos2\theta_0 + H\cos(\theta_H-\theta_0))}H_{DL} - \frac{I_{AC}R_{PHE}\sin^2\theta_0\cos\varphi_H}{H\sin\theta_H}(H_{FL}+H_{Oe}). \quad (1)$$

Here, R_{AHE} and R_{PHE} are the anomalous Hall and planar Hall resistances, respectively. θ_0 is the polar angle of the magnetization and can be obtained from the first harmonic Hall voltage $V_\omega = I_{AC}R_{AHE}\cos\theta_0$. H_{Oe} is the Oersted field produced by the current, and H_K is the effective out-of-plane anisotropy field. θ_H and φ_H are the polar and azimuthal angles of the direction of the applied magnetic field, respectively. A notable feature of Eq. (1) is that while the second term, the H_{FL} contribution, has an inverse H dependence, the H_{DL} contribution in the first term peaks when H is comparable to $-H_K$, i.e., when the applied field compensates the shape anisotropy and the DL SOT becomes more effective at driving the magnetization oscillation. Importantly, an out-of-plane temperature gradient generally exists in harmonic Hall measurements because of significant Joule heating, and while harmonic Hall measurements with a rotating in-plane magnetic field need to account for thermoelectric effects [21,22], the measurement of $V_{2\omega}$ when the magnetic field is applied

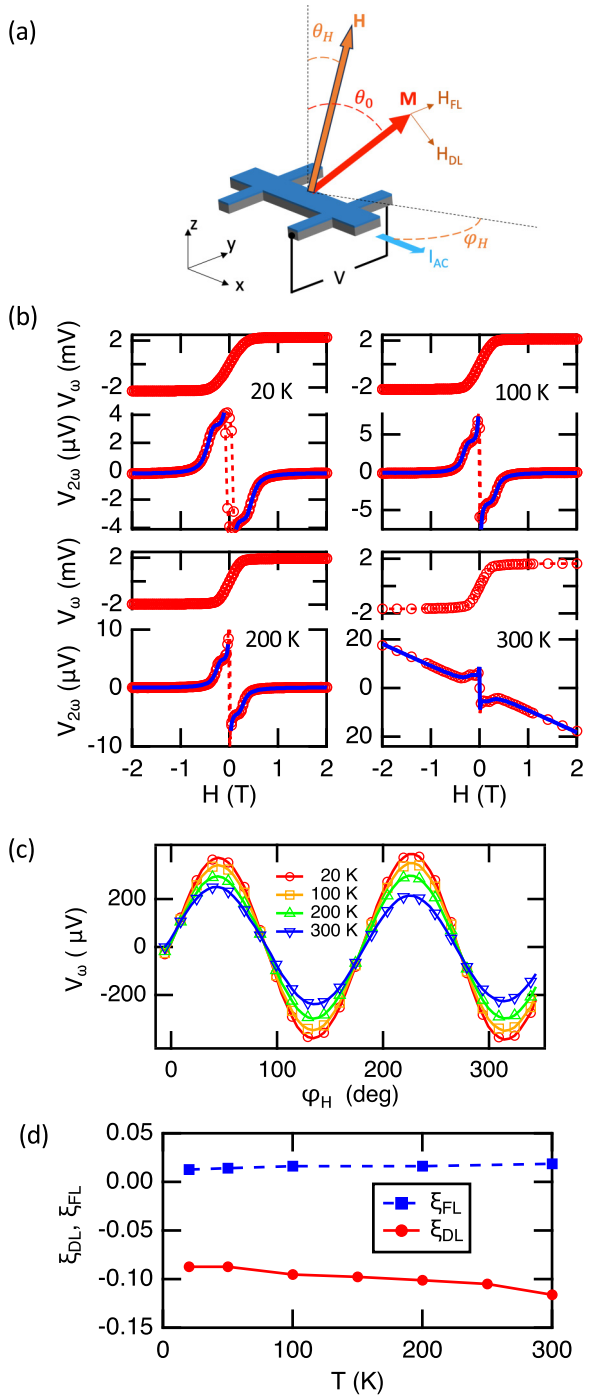

FIG. 6. (a) Schematic of the harmonic Hall measurement. (b) Field dependence of the first and second harmonic Hall voltages of a Ta_3Sb(9.5 nm)/CFB(1 nm) device measured at various temperatures. The solid lines are curve fits. (c) The first harmonic Hall voltage as a function of the azimuthal angle for the same device measured with an in-plane field. (d) Temperature dependence of the DL and FL SOT efficiencies.

out-of-plane is not susceptible to the out-of-plane temperature gradient.

Figure 6(b) shows the first harmonic V_ω and second harmonic $V_{2\omega}$ Hall voltages of a Ta_3Sb(9.5 nm)/CFB(1 nm) bilayer measured as a function of the applied out-of-plane magnetic field H at various temperatures. The offsets due to Hall-lead misalignment and the linear backgrounds due to the ordinary Hall effect have been removed from the V_ω data, whereas no processing has been done on the $V_{2\omega}$ data. The sample has in-plane magnetization. The applied AC current is $I_{AC} = 3$ mA. The applied field is intentionally tilted by 5° away from the surface normal to avoid domain formation (i.e., $\theta_H = 5°$ when $\varphi_H = \pi$ or $\theta_H = 85°$ when $\varphi_H = 0$). With an increasing out-of-plane field, the V_ω curves show the magnetization being pulled out of plane, reaching saturation when the applied field overcomes the effective in-plane anisotropy. From the V_ω curves, R_{AHE} and H_K can be determined. H_K is the field at which a line extrapolated from the initial rise of V_ω intersects the saturation. $|H_K|$ at 300 K is 0.17 T, which is significantly lower than the demagnetizing field $4\pi M_s = 1.5$ T for CFB because of the presence of a perpendicular magnetic anisotropy at the CFB/MgO interface. Here, M_s is the saturation magnetization of a single CFB layer measured using vibrating sample magnetometry. We also separately measured V_ω while rotating the applied field in the sample plane, as shown in Fig. 6(c), and determined R_{PHE}. In Fig. 6(b), the $V_{2\omega}$ curves exhibit bumps which clearly signify the presence of DL SOT and, for $T \leqslant 200$ K, asymptote towards zero. For higher temperatures, such as the $T = 300$ K case shown, the $V_{2\omega}$ curves have linear-in-H backgrounds, which we attribute to the ordinary Nernst effect arising from *in-plane* temperature gradients due to lateral asymmetries of the Hall bar structure. With R_{AHE}, R_{PHE}, and θ_0 determined, we extracted H_K, H_{DL}, and H_{FL} by fitting the nonhysteretic portions of the $V_{2\omega}$ curves with Eq. (1). The H_K values from the curve fits agree well with the saturation fields obtained from the V_ω curves.

The efficiencies at which the current generates DL and FL SOTs (ξ_{DL} and ξ_{FL}) are given by equating the transferred angular momentum from the spin current with the effect of H_{DL} and H_{FL} on the magnetization [23]:

$$\xi_{DL(FL)} = \frac{2e\mu_0 M_s t H_{DL(FL)}}{\hbar j_c}, \tag{2}$$

where t is the thickness of the ferromagnetic CFB layer. Using $M_s = 1.19$ MA/m, we determined ξ_{DL} and ξ_{FL} of the Ta_3Sb films. Figure 6(d) summarizes ξ_{DL} and ξ_{FL} at various temperatures. ξ_{DL} and ξ_{FL} are opposite in sign. ξ_{DL} decreases from -0.087 at 20 K to -0.116 at 300 K, while ξ_{FL} increases from 0.013 at 20 K to 0.019 at 300 K.

On the other hand, in an ST-FMR measurement, the RF current produces high frequency SOTs which excite resonant oscillation of the magnetization at the resonant frequency f_{res} and the resonant field H_{res} [18]. We applied RF excitations to Ta_3Sb/Py bilayer structures at frequencies from 4 GHz to 10 GHz and measured V_{mix} while sweeping the applied magnetic field. The RF power was kept constant at 11.5 dBm. The mixing of the RF current and current-induced RF anisotropic magnetoresistance gives rise to a DC voltage V_{mix}, which consists of symmetric and antisymmetric Lorentzian components with magnitudes of S and A, respectively:

$$V_{\text{mix}} = S\frac{\Delta H^2}{\Delta H^2 + (H - H_{\text{res}})^2} + A\frac{\Delta H(H - H_{\text{res}})}{\Delta H^2 + (H - H_{\text{res}})^2}. \tag{3}$$

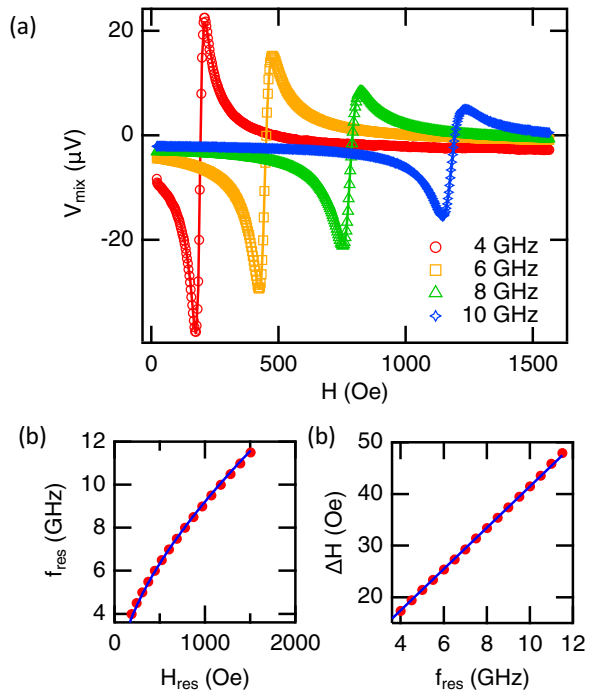

FIG. 7. (a) ST-FMR spectra of a Ta_3Sb(9.5 nm)/Py(5 nm) sample measured at various frequencies. (b) The resonant frequency as a function of the magnetic field. The solid line is a fit using the Kittel formula. (c) Half linewidth of the ST-FMR spectra as a function of the resonant frequency. The solid line is a linear fit.

Here, ΔH is half of the linewidth, S is proportional to H_{DL}, and A is proportional to $H_{FL} + H_{Oe}$. The DL SOT efficiency is, thus, given by [24]:

$$\xi_{DL} = \frac{S}{A}\frac{e\mu_0 M_s t d}{\hbar}\sqrt{1+\frac{4\pi M_{\text{eff}}}{H_{\text{res}}}}\left(1+\frac{\hbar\xi_{FL}}{e\mu_0 M_s t d}\right). \quad (4)$$

Here, t and d are the thicknesses of the Py and Ta_3Sb layers, respectively, and M_{eff} is the effective magnetization of Py.

Figure 7(a) shows typical ST-FMR spectra for a Ta_3Sb(9.5 nm)/Py(5 nm) bilayer measured at 300 K. The values of H_{res}, ΔH, S, and A are obtained by fitting the ST-FMR spectra using Eq. (3). As shown in Fig. 7(b), by fitting the resonant frequency f_{res} as a function of H_{res} using the Kittel formula $f_{\text{res}} = (\gamma/2\pi)[H_{\text{res}}(H_{\text{res}} + 4\pi M_{\text{eff}})]^{1/2}$ and $\gamma = 1.855\times10^{11}$ Hz/T [25], we obtain $M_{\text{eff}} = 697$ kA/m. The value of M_{eff} is similar to that of $M_s = 716$ kA/m for the Py layer, determined from vibrating sample magnetometry. With ST-FMR alone, ξ_{DL} and ξ_{FL} cannot be independently determined without fabricating a series of bilayers with different d or t while maintaining consistent qualities for the layers and interfaces. Nevertheless, given that ξ_{FL} is an intrinsic quantity, we can take the value of ξ_{FL} determined from harmonic Hall measurements on Ta_3Sb/CFB. Using $\xi_{FL} = 0.019$ in Eq. (4), we obtain the average $\xi_{DL} = -0.098$ for Ta_3Sb/Py, which is quite close to the $\xi_{DL} = -0.116$ obtained for Ta_3Sb/CFB.

The SOT efficiency ξ is given by the intrinsic spin Hall angle θ_{SH} and the interfacial spin transparency T_{int} via $\xi = T_{\text{int}}\theta_{SH}$. The values of $|\xi_{DL}|$ can be considered as the lower bound for $|\theta_{SH}|$ in the event of a spin-transparent interface, i.e., when $T_{\text{int}} = 1$. However, T_{int} is generally less than unity at realistic interfaces due to spin mixing [24,26,27]:

$$T_{\text{int}} = 2g_{\text{eff}}^{\uparrow\downarrow}/[(h/e^2)G_{NM}], \quad (5)$$

where $g_{\text{eff}}^{\uparrow\downarrow}$ is the effective spin mixing conductance, $G_{NM} = \sigma/\lambda$ is the spin conductance of the Ta_3Sb layer, and λ is the spin diffusion length. Equation (5) is valid when the Ta_3Sb layer thickness is far greater than λ [24]. Given that the Ta_3Sb layer is in the Mott-Ioffe-Regel limit, it is reasonable to assume this condition is satisfied. We evaluate $g_{\text{eff}}^{\uparrow\downarrow}$ from linewidth broadening in the ST-FMR spectra, because spin mixing enhances the Gilbert damping [28,29]: $\Delta\alpha = \alpha - \alpha_0 = (\frac{\gamma\hbar}{4\pi M_s t_{Py}})g_{\text{eff}}^{\uparrow\downarrow}$. Figure 7(c) shows the half linewidth ΔH extracted from the ST-FMR spectra as a function of the resonant frequency f_{res}. Fitting the data points with the linear relation $\Delta H = (2\pi\alpha/\gamma)f_{\text{res}} + \Delta H_0$ yields the Gilbert damping parameter $\alpha = 0.0118$. Using $\alpha_0 = 0.0090$ measured from a sputtered Py single layer [30], we obtain $g_{\text{eff}}^{\uparrow\downarrow} = 6.48\times10^{18}$ m^{-2}. Since the disorder in the sputtered A15 Ta_3Sb films is primarily the replacement of Sb atoms by Ta atoms at the Sb sites, we take the shortest physical length scale that may correspond to spin flip scattering, i.e., the closest distance between two Sb sites ($a\sqrt{3}/2$), as the lower bound for λ to estimate the lower bound for T_{int}. This yields the lower bound of 0.43 for T_{int} at the Ta_3Sb/Py interface and, thus, the upper bound for $|\theta_{SH}|$ is 0.230. Therefore, the A15 Ta_3Sb has an intrinsic spin Hall angle θ_{SH} in the range of -0.098 to -0.230, and its spin Hall conductivity σ_{SH} is in the range of -526 to $-1230(\hbar/e)$ S/cm.

V. ELECTRONIC STRUCTURE

We note that the wide ranges for θ_{SH} and σ_{SH} are due to uncertainties in the interfacial spin transparency T_{int}. Nevertheless, even with our conservative estimate of λ, the maximum possible value for $|\sigma_{SH}|$ in the sputtered A15 Ta_3Sb thin film is smaller than the theoretical prediction of 1400 $(\hbar/e)$ S/cm. The discrepancy may be explained by the fact that the theoretical prediction is based on band structure calculations for the stoichiometric A15 Ta_3Sb, while our thin films of A15 Ta_3Sb—as well as bulk crystals of A15 Ta_3Sb—are stabilized with the chemical composition of Ta:Sb $\sim$ 4:1 (or, $Ta_{3.2}Sb_{0.8}$, to emphasize the replacement of 20% Sb by Ta due to site-mixing [10]). To examine the effect of off-stoichiometry on spin Hall conductivity, we performed first-principles density functional theory (DFT) calculations to evaluate changes in the Fermi energy E_F as a result of electron doping from the excess Ta atoms.

We start by calculating the band structure of the stoichiometric A15 Ta_3Sb using the projector augmented wave (PAW) method as implemented in the Vienna Ab initio Simulation Package (VASP) code [31,32]. We converge the DFT calculations using a $10\times10\times10$ k-mesh and an energy cutoff of 400 eV for the plane-wave basis. We use the Perdew-Burke-Ernzerhof (PBE) functional for the exchange and correlation energy of DFT. Figure 8(a) shows the PBE band structure calculated with SOC included. It is in excellent agreement with that of Ref. [5]. We then evaluate E_F for different num-

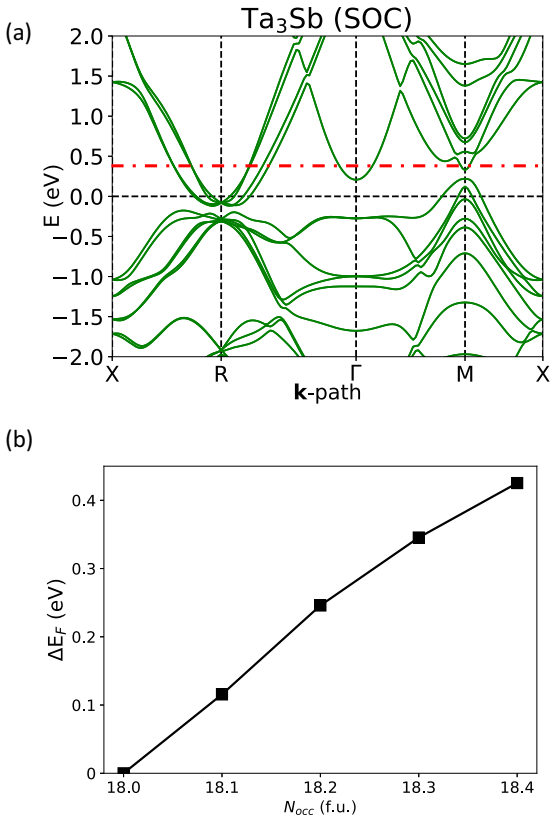

FIG. 8. (a) Calculated band structure of Ta_3Sb with SOC included. The dot-dash line indicates the Fermi level when 20% of Sb is replaced by Ta. (b) The change in E_F plotted as a function of the occupancy number for Ta_3Sb.

bers of occupied electrons (N_{occ}), assuming that the band structure is shifted rigidly (the Kohn-Sham eigenvalues are fixed) and only E_F is changed due to doping. We recompute the Kohn-Sham equation for each N_{occ}, while fixing the charge density obtained from the converged solution during iterations to impose the same band structure. For the summation of the occupied bands and k-points below E_F, we adopt the tetrahedron method using the $10\times10\times10$ k-mesh. The resulting change in E_F (ΔE_F) as a function of N_{occ} per formula unit (f.u.) is shown in Fig. 8(b). $Ta_{3.2}Sb_{0.8}$ has 0.4 more valence electrons per formula unit than Ta_3Sb; we estimate that the extra electrons increase E_F by 0.425 eV and, according to Fig. 4C of Ref. [5], would move σ_{SH} off its peak to ~ -900 $(\hbar/e)$ S/cm. This reduced value falls within our estimated range for σ_{SH} in the sputtered A15-phase Ta_3Sb thin films.

VI. DISCUSSION AND SUMMARY

That the shift of E_F away from the SOC-gapped Dirac crossings leads to a reduced σ_{SH} in the off-stoichiometric A15-phase Ta_3Sb validates the strategy by Derunova *et al.* [5] of searching for high σ_{SH} in A15 compounds due to their symmetry, in the same way that Ta-doped W exhibiting enhanced σ_{SH} [6,7] does. The opposite end results of these two scenarios, however, underscore the importance of the E_F of the actual realizable material, since many of the A15 compounds are stable only in compositions that are different from the ideal stoichiometry [33,34]. To maximize σ_{SH}, it might be beneficial to investigate pseudo-binary A15 alloys, such as Ta_3(Sb, Sn), where the Sn dopant could take up the excess electrons and return E_F to the optimum level. On the other hand, we note that even with the raised E_F in the off-stoichiometric A15 Ta_3Sb, the topological surface states are still accessible [5,8], making the A15 Ta_3Sb thin films potentially useful for exploring topological superconductivity.

In summary, we have synthesized single-phase A15 Ta_3Sb thin films by co-sputtering. The phase-locking growth mechanism allows for facile and direct synthesis. However, the A15 Ta_3Sb is stabilized at a composition that is different from the ideal stoichiometry. This leads to the shift of the Fermi level away from the SOC-gapped Dirac crossings, where the maximum spin Hall conductivity is expected. It is, therefore, important to note the thermodynamic constraints of materials synthesis. A possible approach to designing giant spin-Hall-effect A15 compounds may lie in tuning the Fermi level via pseudo-binary alloys.

ACKNOWLEDGMENTS

We acknowledge Dr. Timothy Spila for the acquisition of RBS data. Work at Argonne National Laboratory, including film growth and structural characterization, transport measurements, and theoretical calculations, was supported by the U.S. Department of Energy Office of Science, Basic Energy Sciences, Materials Science and Engineering Division. The use of the microscopy and microfabrication facilities at the Center for Nanoscale Materials was supported by the U.S. DOE, BES under Contract No. DE-AC02-06CH11357. H.P. acknowledges the computing resources provided on Bebop, a high-performance computing cluster operated by the Laboratory Computing Resource Center at Argonne National Laboratory. The ST-FMR experiments at Argonne National Laboratory was supported by the U.S. DOE, Office of Science, Basic Energy Sciences, Materials Sciences and Engineering Division under Contract No. DE-SC0022060.

[1] I. M. Miron, G. Gaudin, S. Auffret, B. Rodmacq, A. Schuhl, S. Pizzini, J. Vogel, and P. Gambardella, Current-driven spin torque induced by the Rashba effect in a ferromagnetic metal layer, Nat. Mater. **9**, 230 (2010).

[2] L. Liu, O. J. Lee, T. J. Gudmundsen, D. C. Ralph, and R. A. Buhrman, Current-induced switching of perpendicularly magnetized magnetic layers using spin torque from the spin Hall effect, Phys. Rev. Lett. **109**, 096602 (2012).

[3] Q. Shao, P. Li, L. Liu, H. Yang, S. Fukami, A. Razavi, H. Wu, K. Wang, F. Freimuth, Y. Mokrousov, M. D. Stiles, S. Emori, A. Hoffmann, J. Åkerman, K. Roy, J.-P. Wang, S.-H. Yang, K. Garello, and W. Zhang, Roadmap of spin–orbit torques, IEEE Trans. Magn. **57**, 800439 (2021).

[4] G. Y. Guo, S. Murakami, T.-W. Chen, and N. Nagaosa, Intrinsic spin Hall effect in platinum: First-principles calculations, Phys. Rev. Lett. **100**, 096401 (2008).

[5] E. Derunova, Y. Sun, C. Felser, S. S. P. Parkin, B. Yan, and M. N. Ali, Giant intrinsic spin Hall effect in W_3Ta and other A15 superconductors, Sci. Adv. **5**, eaav8575 (2019).

[6] M. Z. Minhas, A. K. Pandeya, B. Grover, A. Fumarola, I. Kostanovskiy, B. K. Hazra, W. Hoppe, G. Woltersdorf, A. Bedoya-Pinto, S. S. P. Parkin, and M. N. Ali, Doping-induced spin Hall ratio enhancement in A15-phase, Ta-doped β-W thin films, J. Phys. Mater. **3**, 044001 (2020).

[7] J.-Y. Kim, D.-S. Han, M. Vafaee, S. Jaiswal, K. Lee, G. Jakob, and M. Kläui, Enhancement of spin Hall conductivity in W–Ta alloy, Appl. Phys. Lett. **117**, 142403 (2020).

[8] M. Kim, C.-Z. Wang, and K.-M. Ho, Topological states in A15 superconductors, Phys. Rev. B **99**, 224506 (2019).

[9] R. M. Sattigeri, G. Cuono, G. Hussain, X. Ming, A. Di Bernardo, C. Attanasio, M. Cuoco, and C. Autieri, Dirac surface states, multiorbital dimerization, and superconductivity in Nb- and Ta-based A15 compounds, Phys. Rev. B **109**, 075119 (2024).

[10] R. Chapai, A. Rydh, M. P. Smylie, D. Y. Chung, H. Zheng, A. E. Koshelev, J. E. Pearson, W.-K. Kwok, J. F. Mitchell, and U. Welp, Superconducting properties of the spin Hall candidate Ta_3Sb with eightfold degeneracy, Phys. Rev. B **105**, 184510 (2022).

[11] F. Failamani, P. Broz, D. Macciò, S. Puchegger, H. Müller, L. Salamakha, H. Michor, A. Grytsiv, A. Saccone, E. Bauer, G. Giester, and P. Rogl, Constitution of the systems {V,Nb,Ta}-Sb and physical properties of di-antimonides $\{V,Nb,Ta\}Sb_2$, Intermetallics **65**, 94 (2015).

[12] L. Allen, M. Beasley, R. Hammond, and J. Turneaure, RF surface resistance of Nb3Sn, NbZr, and NbN thin films, IEEE Trans. Magn. **23**, 1405 (1987).

[13] O. Gunnarsson, M. Calandra, and J. E. Han, *Colloquium:* Saturation of electrical resistivity, Rev. Mod. Phys. **75**, 1085 (2003).

[14] P. A. Lee and T. V. Ramakrishnan, Disordered electronic systems, Rev. Mod. Phys. **57**, 287 (1985).

[15] S. Ciuchi, D. Di Sante, V. Dobrosavljević, and S. Fratini, The origin of Mooij correlations in disordered metals, Npj Quantum Mater. **3**, 44 (2018).

[16] J. H. Mooij, Electrical conduction in concentrated disordered transition metal alloys, Phys. Status Solidi (A) **17**, 521 (1973).

[17] M. Hayashi, J. Kim, M. Yamanouchi, and H. Ohno, Quantitative characterization of the spin-orbit torque using harmonic Hall voltage measurements, Phys. Rev. B **89**, 144425 (2014).

[18] L. Liu, T. Moriyama, D. C. Ralph, and R. A. Buhrman, Spin-torque ferromagnetic resonance induced by the spin Hall effect, Phys. Rev. Lett. **106**, 036601 (2011).

[19] Y. Li, F. Zeng, S. S.-L. Zhang, H. Shin, H. Saglam, V. Karakas, O. Ozatay, J. E. Pearson, O. G. Heinonen, Y. Wu, A. Hoffmann, and W. Zhang, Giant anisotropy of Gilbert damping in epitaxial CoFe films, Phys. Rev. Lett. **122**, 117203 (2019).

[20] Y. Li, H. Saglam, Z. Zhang, R. Bidthanapally, Y. Xiong, J. E. Pearson, V. Novosad, H. Qu, G. Srinivasan, A. Hoffmann, and W. Zhang, Simultaneous optical and electrical spin-torque magnetometry with phase-sensitive detection of spin precession, Phys. Rev. Appl. **11**, 034047 (2019).

[21] C. O. Avci, K. Garello, M. Gabureac, A. Ghosh, A. Fuhrer, S. F. Alvarado, and P. Gambardella, Interplay of spin-orbit torque and thermoelectric effects in ferromagnet/normal-metal bilayers, Phys. Rev. B **90**, 224427 (2014).

[22] N. Roschewsky, E. S. Walker, P. Gowtham, S. Muschinske, F. Hellman, S. R. Bank, and S. Salahuddin, Spin-orbit torque and Nernst effect in Bi-Sb/Co heterostructures, Phys. Rev. B **99**, 195103 (2019).

[23] A. V. Khvalkovskiy, V. Cros, D. Apalkov, V. Nikitin, M. Krounbi, K. A. Zvezdin, A. Anane, J. Grollier, and A. Fert, Matching domain-wall configuration and spin-orbit torques for efficient domain-wall motion, Phys. Rev. B **87**, 020402(R) (2013).

[24] C.-F. Pai, Y. Ou, L. H. Vilela-Leão, D. C. Ralph, and R. A. Buhrman, Dependence of the efficiency of spin Hall torque on the transparency of Pt/ferromagnetic layer interfaces, Phys. Rev. B **92**, 064426 (2015).

[25] J. M. Shaw, H. T. Nembach, T. J. Silva, and C. T. Boone, Precise determination of the spectroscopic *g*-factor by use of broadband ferromagnetic resonance spectroscopy, J. Appl. Phys. **114**, 243906 (2013).

[26] P. M. Haney, H.-W. Lee, K.-J. Lee, A. Manchon, and M. D. Stiles, Current induced torques and interfacial spin-orbit coupling: Semiclassical modeling, Phys. Rev. B **87**, 174411 (2013).

[27] Y.-T. Chen, S. Takahashi, H. Nakayama, M. Althammer, S. T. B. Goennenwein, E. Saitoh, and G. E. W. Bauer, Theory of spin Hall magnetoresistance, Phys. Rev. B **87**, 144411 (2013).

[28] Y. Tserkovnyak, A. Brataas, G. E. W. Bauer, and B. I. Halperin, Nonlocal magnetization dynamics in ferromagnetic heterostructures, Rev. Mod. Phys. **77**, 1375 (2005).

[29] W. Zhang, W. Han, X. Jiang, S.-H. Yang, and S. S. P. Parkin, Role of transparency of platinum–ferromagnet interfaces in determining the intrinsic magnitude of the spin Hall effect, Nat. Phys. **11**, 496 (2015).

[30] D. Hong, N. Anand, C. Liu, H. Liu, I. Arslan, J. E. Pearson, A. Bhattacharya, and J. S. Jiang, Large anomalous Nernst and inverse spin-Hall effects in epitaxial thin films of kagome semimetal Mn_3Ge, Phys. Rev. Mater. **4**, 094201 (2020).

[31] G. Kresse and J. Furthmuller, Efficient iterative schemes for *ab initio* total-energy calculations using a plane-wave basis set, Phys. Rev. B **54**, 11169 (1996).

[32] G. Kresse and D. Joubert, From ultrasoft pseudopotentials to the projector augmented-wave method, Phys. Rev. B **59**, 1758 (1999).

[33] J. Muller, A15-type superconductors, Rep. Prog. Phys. **43**, 641 (1980).

[34] R. Chapai, M. P. Smylie, H. Hebbeker, D. Y. Chung, W.-K. Kwok, J. F. Mitchell, and U. Welp, Superconducting properties and gap structure of the topological superconductor candidate Ti_3Sb, Phys. Rev. B **107**, 104504 (2023).